# Penrose high-dynamic-range imaging

**Jia Li,[a,*] Chenyan Bai,[a] Zhouchen Lin,[b,c] and Jian Yu[a]**
[a]Beijing Jiaotong University, Beijing Key Laboratory of Traffic Data Analysis and Mining, School of Computer and Information Technology, Beijing 100044, China
[b]Peking University, Key Laboratory of Machine Perception (MOE), School of Electronic Engineering and Computer Science, Beijing 100871, China
[c]Shanghai Jiao Tong University, Cooperative Medianet Innovation Center, Shanghai 200240, China

**Abstract.** High-dynamic-range (HDR) imaging is becoming increasingly popular and widespread. The most common multishot HDR approach, based on multiple low-dynamic-range images captured with different exposures, has difficulties in handling camera and object movements. The spatially varying exposures (SVE) technology provides a solution to overcome this limitation by obtaining multiple exposures of the scene in only one shot but suffers from a loss in spatial resolution of the captured image. While aperiodic assignment of exposures has been shown to be advantageous during reconstruction in alleviating resolution loss, almost all the existing imaging sensors use the square pixel layout, which is a periodic tiling of square pixels. We propose the Penrose pixel layout, using pixels in aperiodic rhombus Penrose tiling, for HDR imaging. With the SVE technology, Penrose pixel layout has both exposure and pixel aperiodicities. To investigate its performance, we have to reconstruct HDR images in square pixel layout from Penrose raw images with SVE. Since the two pixel layouts are different, the traditional HDR reconstruction methods are not applicable. We develop a reconstruction method for Penrose pixel layout using a Gaussian mixture model for regularization. Both quantitative and qualitative results show the superiority of Penrose pixel layout over square pixel layout. *© 2016 SPIE and IS&T* [DOI: 10.1117/1.JEI.25.3.033024]

Keywords: Penrose; high-dynamic-range imaging; spatially varying exposures; Gaussian mixture models.
Paper 16074 received Jan. 27, 2016; accepted for publication Jun. 2, 2016; published online Jun. 23, 2016.

## 1 Introduction

The real scene has a huge dynamic range that cannot be completely captured by a traditional imaging sensor in a single exposure. Namely, with a high exposure, the obtained image will be saturated in the bright scene areas but captures the dark regions well. In contrast, the image taken with a low exposure will have less saturation in the bright regions but will be too noisy in the dark areas. As a result, the image captured by a traditional imaging sensor often contains improperly exposed pixels that are either saturated or too noisy, where the brightness information is lost. Such images are called low-dynamic-range (LDR) images. High-dynamic-range (HDR) imaging aims to enhance the dynamic range of traditional imaging sensors by hardware modifications or merging multiple LDR images captured with varying exposures.[1]

Most of the literature to date focuses on the multishot HDR approach.[2–17] It sequentially takes multiple LDR images of the scene with different exposures and then combines them to produce an HDR image. Due to the need for capturing multiple exposures, the image capture process inevitably takes a long time, making it challenging to combine LDR images captured in the presence of camera and object movements. When the camera moves during capture, an alignment of differently exposed images is needed, which remains a difficult task.[4,5,6,18] Moreover, when there are moving objects in the scene, ghosting artifacts will be introduced in the reconstructed HDR image,[17,19,20] which degrade the image quality greatly.[13] Additionally, multiple images require extra storage.

To handle these difficulties, the spatially varying exposures (SVE) technology obtains multiple exposures in a single image.[21] Since all exposures are captured simultaneously, the alignment and deghosting operations for the dynamic scenes are naturally avoided. Also, one only needs to store a single image for reconstructing an HDR image. Because of these benefits, the SVE technology has been applied in commercial products. For example, Fujifilm[22] designed the fourth Generation Super CCD that uses paired octagonal pixels with different light sensitivities [Fig. 2(a)]. The larger pixel is likely saturated, whereas the smaller one is not. This results in different exposures in a single shot. Sony[23] proposed setting a long and a short exposure times to two groups of pixels, respectively [Fig. 2(b)]. Note that the SVE technology can be accomplished via many ways, e.g., placing an optical mask with spatially varying sensitivities over a traditional imaging sensor,[21,24,25] setting SVE times to pixels,[23,26,28,29] or directly using pixels with different light sensitivities.[22] All these implementations result in the same effect, i.e., an imaging sensor with SVE. So in this work, we consider only using optical masks to achieve the SVE technology, which we call SVE arrays [Figs. 1(b) and 1(c)], where brighter pixels have a higher light sensitivity and the darker ones have a lower sensitivity. The obtained raw images with an SVE array are called SVE images [Figs. 1(d) and 1(e)], which have SVE of the scene according to the SVE array. Then, HDR images are estimated from

*Address all correspondence to: Jia Li, E-mail: jiali.gm@gmail.com

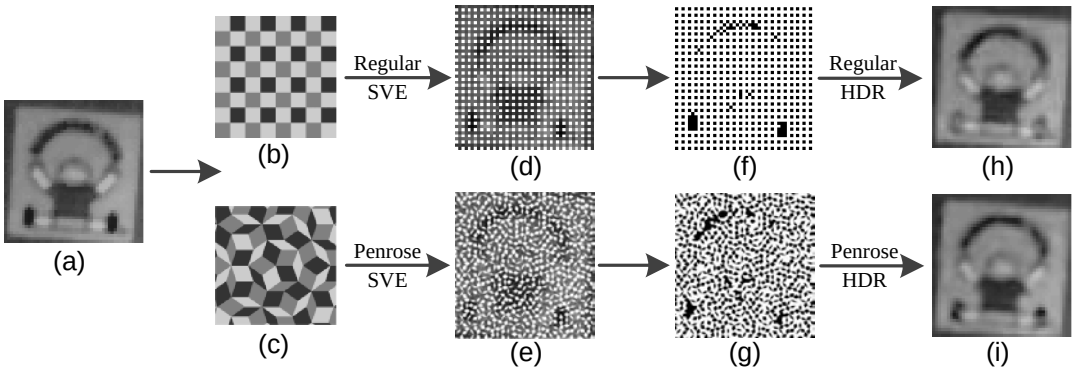


**Fig. 1** Comparison of Penrose and regular SVE imaging. Note the feet of the cartoon character. More comparisons are shown in Figs. 10–13. (a) An HDR image to simulate a real scene, (b) regular SVE array based on the Bayer CFA,[30] where three colors are replaced by three different sensitivities, (c) Penrose SVE array with three different sensitivities, (d) regular SVE image, (e) Penrose SVE image, (f) and (g) are the proper exposure masks to identify the properly exposed pixels (white) and the improperly exposed ones (black) in the regular and Penrose SVE images, respectively, (h) regular HDR image, and (i) Penrose HDR image. Note that all HDR images shown in this paper are rendered by using MATLAB®'s defult tonemap function.

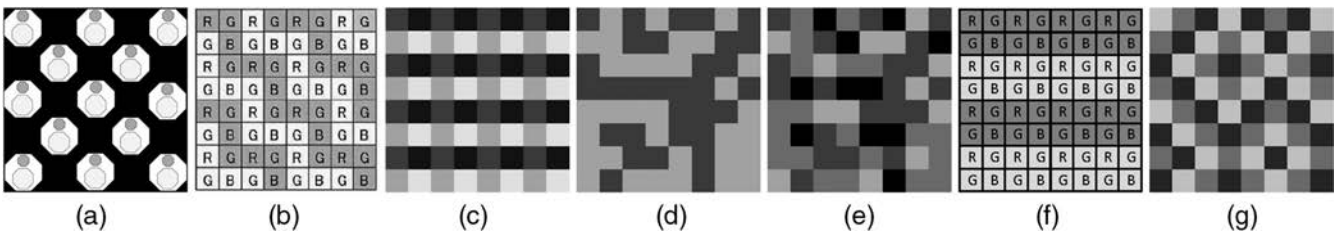


**Fig. 2** SVE sensors and regular and random SVE arrays. (a) Fujifilm's fourth Generation Super CCD,[22] (b) Sony SVE sensor,[23] (c) regular SVE array with four different sensitivities,[21] (d) random SVE array with two different sensitivities,[24] (e) random SVE array with four different sensitivities,[25] (f) CFA with row-wise varying sensitivities,[26] and (g) random SVE array based on the random CFA,[27] where three colors are replaced by three different sensitivities.

SVE images by the HDR reconstruction methods [Figs. 1(i) and 1(h)].

The main idea of SVE imaging is to achieve higher dynamic range at the cost of spatial resolution.[31] The reduction of spatial resolution results from the following fact. The SVE image regions that correspond to the bright scene areas can only be well exposed at the pixels with a low sensitivity and will be saturated at those with a high sensitivity. In contrast, pixels for the dark scene areas can only be properly exposed with a high sensitivity. Those improperly exposed pixel values in the SVE images are unreliable, which should be regarded as unknown and need to be estimated by an HDR reconstruction method. Therefore, both the SVE array and the reconstruction method affect the spatial resolution of the produced HDR images. As a reconstruction method takes SVE images as input, one can design the SVE array to make the subsequent reconstruction more resistant to resolution reduction.

However, the study of designing SVE arrays has received considerably less attention. Only a few literatures consider this problem.[21,24,32,33] There are two aspects for the design of SVE arrays. The first one is the number of sensitivities used. The more sensitivities used, the wider of dynamic range that could be achieved. But a larger number of used sensitivities will give a lower sampling rate at each sensitivity, which is a trade-off between the spatial and brightness resolutions. So the choice of used sensitivities is only meaningful for a specific application.[24] Typically, one can use two to four different sensitivities.[21,24,32] The second one is the assignment of sensitivities (e.g., periodic or aperiodic). Nayar and Mitsunaga[21] used a regular SVE array periodically tiled by a $2 \times 2$ pattern [Fig. 2(c)]. Based on the difference of color filters in sensitivity of monochrome light, Konnik et al.[32] regarded the regular Bayer color filter array (CFA)[30] as an SVE array for monochrome imaging [Fig. 1(b)]. Hirakawa and Simon,[33] on the other hand, performed HDR color imaging with only the Bayer CFA. They argued that different light sensitivities are already implied by the Bayer CFA, which can be further magnified by using carefully selected photographic filters. Motivated by the spatial aliasing problem of regular sampling, Schöberl et al.[24] used a random SVE array, which assigns sensitivities aperiodically [Fig. 2(d)]. Their experiments showed that a random SVE array preforms better than a regular one during the subsequent reconstruction in mitigating resolution reduction. Note that spatial aliasing is an effect that high spatial frequencies in the original signal appear as low spatial frequencies in the spatially sampled signal, making the faithful reconstruction of the original signal difficult.[34] This implies that reducing

aliasing in the sampled image can greatly enhance the possibility of reconstructing the original one, thereby improving the spatial resolution of the reconstructed image. The capability of nonregular sampling in reducing aliasing has also been testified by other spatial sampling arrays, e.g., halftone mask[35] or CFA.[27] However, all of them use the square pixel layout (square layout for short), i.e., periodic tiling of square pixels.

Some researches in visual physiology have shown that the irregularity in a sampling array greatly reduces aliasing caused by undersampling.[36,37] Inspired by these studies, we present the Penrose pixel layout (Penrose layout for short), an irregular pixel layout in rhombus Penrose tiling,[38] for HDR imaging. Rhombus Penrose tiling is an aperiodic tiling, which tiles the plane in a nonperiodic manner.[38] So, with an SVE array, the Penrose layout has both exposure and pixel aperiodicities. Moreover, rhombus Penrose tiling uses only two kinds of rhombi, having equal sides but different angles [see Fig. 1(c)]. Thus, the manufacture of the Penrose layout is much easier than those of completely irregular layouts (e.g., Voronoi tessellation[39]) (although not as easy as square layouts), which has been discussed in detail.[40] The superiority of the Penrose layout over square layout has been tested on superresolution[40] and demosaicking.[41] However, super-resolution trades off temporal resolution for spatial resolution, whereas demosaicking trades off spatial resolution for spectral resolution.[31] It is unclear whether we can obtain better HDR images with the Penrose layout using the SVE technology, which trades off spatial resolution for brightness resolution.[31]

The contributions of this paper are as follows:

- We propose the Penrose layout for HDR imaging using the SVE technology. Due to the two aperiodicities of the Penrose layout, the spatial resolution of the reconstructed HDR images can be improved.
- We propose an HDR reconstruction method for the Penrose layout using a Gaussian mixture model[42] for regularization. With the proposed method, we show that the Penrose layout performs better than the square layout in terms of peak signal-to-noise ratio (PSNR) and visual quality. We further testify the effectiveness of irregular pixels for high-quality HDR imaging.

## 2 Related Work

In this section, we first review the most popular multishot HDR imaging. Then we review the existing SVE imaging. We omit other single-shot HDR approaches, e.g., the approaches proposed in Refs. 43 and 44.

### 2.1 *Multishot High-Dynamic-Range Imaging*

Multishot HDR imaging is the most popular HDR approach. It sequentially takes multiple LDR images of the same scene with different exposures and then merges them into a single HDR image. Both Mann and Picard[2] and Debevec and Malik[3] reconstructed an HDR image from multiple LDR images for a static scene with a static camera. Subsequently, there are broad literatures on noise reduction,[8,9] exposure setting,[10–12] image alignment,[4–7] and ghosting removal[13–16] for HDR imaging.

Based on detailed models of noise, Hasinoff et al.[8] and Granados et al.[9] derived the optimal weights for HDR reconstruction. Hirakawa and Wolfe[10] provided a statistical analysis of exposure controls. To better deal with dynamic cameras and objects, Gupta et al.[11] presented using exposure times to capture LDR images that have the Fibonacci property, i.e., each exposure is the sum of previous $N(N > 1)$ exposures. More recently, a new exposure setting method was presented based on the scene information and the camera parameters.[12]

Despite significant progress of multishot approach over the years, capturing in the presence of camera and object movements is still challenging. For a moving camera, global camera motion models can be considered to register LDR images,[4] e.g., translation,[5] rotation,[18] or homography transformation models.[6] Also, the brightness consistency assumption[45] is violated for differently exposed images. Consequently, for robust motion estimation, one can transform the LDR images in the intensity domain to the luminance domain,[46] the gradient domain,[47] or the transformed domain[7] by intensity mapping function.[48]

Without proper treatments in dynamic objects, ghosting artifacts will appear in the produced HDR images.[17] Explicit dynamic object detection is not necessary. One can handle ghosting artifacts by user corrections,[13] iteratively assigning smaller weights to pixels that are likely to correspond to dynamic objects,[14] or producing ghost-free HDR images with a joint bilateral filter approach.[49] Based on the assumption that the underlying background is static, HDR reconstruction can be formulated into a rank minimization problem,[16,19] which represents all dynamic objects as a sparse matrix. Many HDR methods explicitly detect dynamic objects according to certain observations. For example, the dynamic objects can cause inconsistent pixels in patches,[50] superpixels,[51] or gradient changes.[52] The noise distribution of color values can also be used to identify dynamic objects.[53] Recently, the patch-based approach has been explored.[15,20]

### 2.2 *Spatially Varying Exposures Imaging*

As discussed previously, the SVE imaging is much less explored. It is a single-shot HDR approach and, hence, can produce ghost-free HDR images.[21] Although we focus on proposing SVE arrays, we cannot obtain HDR images from the SVE images without reconstruction methods. So we review both the existing SVE arrays and reconstruction methods.

#### 2.2.1 *Spatially varying exposures arrays*

The SVE technology is a general principle and can be implemented via many approaches.[21] They differ in hardware design. In addition to those described in Sec. 1, the SVE technology can also be implemented during the readout of pixel values. For example, the coded reset/readout signals[28] can provide multiple exposures within a single shot. Gu et al.[29] used a coded rolling shutter to obtain multiple exposures simultaneously. Recently, Cho et al.[26] proposed using a coded electronic shutter to acquire row-wise varying exposures in a single image. However, the effects of these approaches can also be achieved by using SVE arrays. For instance, the approach of Cho et al. is equivalent to

using a regular SVE array periodically tiled by a $4 \times 2$ pattern [see Fig. 2(f)].

#### 2.2.2 *Reconstruction methods*

The SVE technology trades spatial resolution for brightness resolution (or dynamic range). To retain the spatial resolution of HDR images, the reconstruction methods need to estimate those improperly exposed pixels. Another important issue of HDR reconstruction is noise reduction, e.g., the photon and photon–electron transfer noise in the SVE images.[54] Furthermore, pixels with a low-sensitivity tend to be quite noisy, particularly those corresponding to the dark scene areas. In general, HDR reconstruction from the SVE images is to inpaint the unknown pixels and denoise the known ones.

Nayar and Mitsunaga proposed two reconstruction methods in Ref. 21. The aggregation method averaged local pixel values of an SVE image to directly get the HDR image. The bicubic interpolation method first discarded the improperly exposed pixels with appropriate thresholds, then it converted pixel values into radiance values through a precomputed response function. It next normalized known radiance values with their respective exposures and then estimated the unknown ones using bicubic interpolation. In Ref. 31, a structural interpolation method was presented. It learned a polynomial function to map an SVE image patch to the center pixel of its corresponding HDR image patch. Konnik et al.[32] first calibrated the sensitivities of color filters in the Bayer CFA. Then, the saturated pixels were estimated from their neighbor pixels. In contrast with the approach of Konnik et al., Hirakawa and Simon[33] considered color HDR imaging. They proposed a demosaicking-inspired algorithm to jointly perform demosaicking and HDR reconstruction from a single image. Schöberl et al.[24] reconstructed HDR images by using the frequency selective extrapolation algorithm.[55] With a detailed modeling of noise, Aguerrebere et al.[25] extended the piecewise linear estimators[56] to perform HDR reconstruction.

## 3 Penrose Pixels for Spatially Varying Exposures Imaging

In this section, we present the Penrose layout for HDR imaging using the SVE technology. We first introduce the process of Penrose SVE imaging. Then, we describe the mapping from the square layout to the Penrose layout. We next present our HDR reconstruction method for the Penrose layout. We use upper and lower case bold letters to denote matrices and vectors, respectively. Images are represented in column vectors.

### 3.1 *Penrose Spatially Varying Exposures Imaging*

As in Ref. 26, we divide the scene into the dark, medium, and bright areas. We use three different sensitivities to account for the three types of scene areas. Then, according to Refs. 21 and 41, we have that monochrome SVE imaging with three sensitivities that can be treated as the mosaicking from a color image consisted of three gray-scale images captured with corresponding exposures, followed by a conversion from radiance values to gray levels. We illustrate the process of Penrose SVE imaging with three sensitivities in Fig. 3. So the model of Penrose SVE imaging is given as follows:

$$\mathbf{p} = f(\mathbf{MTs}) + \mathbf{e}, \tag{1}$$

where $\mathbf{s}$ is the to-be-reconstructed HDR image $\mathbf{T} = (\mathbf{T}_1^T, \mathbf{T}_2^T, \mathbf{T}_3^T)^T$, $\mathbf{T}_i = t_i\mathbf{I}$ is the $i$'th exposure matrix, $\mathbf{I}$ is the identity matrix, $t_i$ is the $i$'th exposure $\mathbf{M} = (\mathbf{M}_1, \mathbf{M}_2, \mathbf{M}_3)$, $\mathbf{M}_i$ is the coefficient matrix of the mapping from the image taken with $t_i$ in the square layout into that in the Penrose layout, which will be described in Sec. 3.2, $\mathbf{e}$ is the noise, e.g., the photon, photon–electron transfer, and

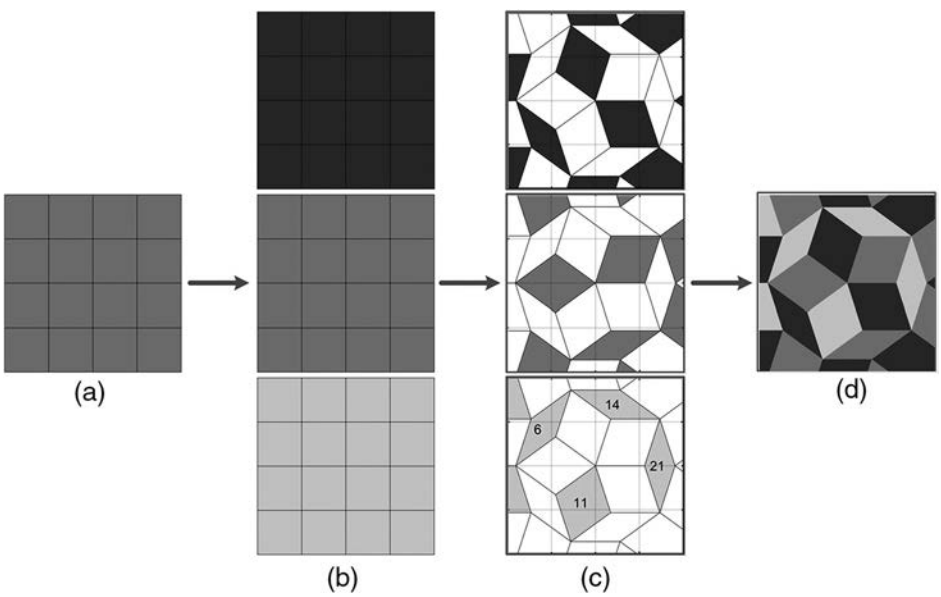


**Fig. 3** Penrose SVE imaging (adapted from Ref. 41, but with a different interpretation). (a) An HDR image, (b) the three different exposures of the original HDR image, (c) the three exposure subimages of Penrose SVE image, in which the white rhombus pixel indicates unrecorded value, and (d) the Penrose SVE image.

quantization noise,[54] and $f(\cdot)$ is the monotonic response function.

As in many works,[24–26,32,33] we use a linear response function for the imaging sensor in the Penrose layout, which implies that $f(\cdot)$ is linear before reaching the saturation threshold. So Eq. (1) can be written as

$$\mathbf{p} = \max[\min(\mathbf{MTs}, B_{\max}), B_{\min}] + \mathbf{e}, \tag{2}$$

where $B_{\min}$ and $B_{\max}$ indicate the minimum and maximum scalar gray levels that the imaging sensor can reliably present, respectively, $\max(\mathbf{x}, B_{\min})$ returns a vector the same size as $\mathbf{x}$ with the largest elements taken from $\mathbf{x}$ or $B_{\min}$, whereas $\min(\mathbf{x}, B_{\max})$ returns the smallest elements taken from $\mathbf{x}$ or $B_{\max}$.

### 3.2 *Mapping the Square Layout into the Penrose Layout*

The explanation of the mapping between square and Penrose layouts has been detailed in Ref. 41. Later, we give a short introduction to it. We take the third mapping between Figs. 3(b) and 3(c) as an example. Since the Penrose and square layouts have different pixel shapes, we first ensure that they have the same resolution, i.e., they have the same number of pixels within the imaging area.[40] Then, we assume that pixels have uniform photosensitivity,[41,57] which implies that the contribution of a Penrose pixel to a square pixel is proportional to its area inside the square pixel and vice versa. So the mapping from the square layout to the Penrose one is given as follows:

$$\mathbf{p}_3 = \mathbf{M}_3\mathbf{r} + \mathbf{e}_3, \tag{3}$$

where $\mathbf{p}_3$ and $\mathbf{r}$ are the column vectors of all the involved Penrose and square pixels, respectively, and $\mathbf{e}_3$ is the noise. The elements of $\mathbf{M}_3$ are the ratios of the areas of the intersections between the two types of pixels to the area of Penrose pixel. Namely

$$\mathbf{M}_3(i,j) = \frac{\mathrm{A}[P_3(i) \cap S_3(j)]}{\mathrm{A}[P_3(i)]},$$

where $P_3(i)$ and $S_3(j)$ are the $i$'th Penrose pixel and the $j$'th square pixel, respectively, and $\mathrm{A}(X)$ represents the area of $X$.

In the third image of Fig. 3(c), there are four Penrose pixels, numbered with 6, 11, 14, and 21, that are completely inside the imaging area of square layout. The corresponding $\mathbf{M}_3$ is shown in Fig. 4. For instance, if one indexes the square layout column-wise, then the Penrose pixel numbered with six covers 0.15, 0.56, 0.22, and 0.07 of the first, second, fifth, and sixth square pixels, respectively.

### 3.3 *Penrose High-Dynamic-Range Model*

We can see from Figs. 1 to 3 that Penrose SVE images are in the Penrose layout, whereas the reconstructed HDR images are in the square layout. So, Penrose HDR reconstruction is inherently more challenging than the square one. The existing HDR reconstruction methods, e.g., bicubic interpolation,[21] frequency selective extrapolation,[24] and the extension of piecewise linear estimators,[25] are limited to the square layout and cannot be directly used to reconstruct HDR images from Penrose SVE images.

Following previous works,[21,24,25] we introduce a proper exposure matrix $\mathbf{U}$ to discard those improperly exposed (saturated or too noisy) pixels, where $\mathbf{U} = \mathrm{diag}(\mathbf{u})$ and $\mathbf{u}$ indicates whether the pixels are properly exposed [see Figs. 1(f) and 1(g)]. Namely

$$\mathbf{u}(i) = \begin{cases} 0, & \text{if } \mathbf{p}(i) \le B_{\min} \quad \text{or} \quad \mathbf{p}(i) \ge B_{\max}, \\ 1, & \text{otherwise.} \end{cases} \tag{4}$$

The model of Penrose SVE imaging in Eq. (2) leads to the following fidelity term for reconstruction of $\mathbf{s}$:

$$L(\mathbf{s}) = \frac{1}{2}\|\mathbf{U}(\mathbf{MTs} - \mathbf{p})\|_2^2. \tag{5}$$

Since $\mathbf{U}$ is not of full column rank, minimizing the fidelity term for $\mathbf{s}$ is ill-posed. To make the optimization tractable, additional image priors must be employed.

The patch-based prior, based on Gaussian mixture models (GMM), has been shown to outperform other generic priors for both denoising and inpainting.[42] The GMM prior captures covariance structure and pixel dependencies over small patches, thereby giving superior performance in modeling the statistics of natural images. This motivates us to use the GMM prior to regularize HDR images. As in Ref. 42, the regularization term for HDR image $\mathbf{s}$ is

$$-\sum_i \log[\mathrm{GMM}(\mathbf{R}_i\mathbf{s})], \tag{6}$$

where $\mathrm{GMM}(\mathbf{R}_i\mathbf{s}) = \sum_{j=1}^{K} \pi_j N(\overline{\mathbf{R}_i\mathbf{s}}; 0, \Sigma_j)$, $K$ is the number of mixture components, $N(0,\cdot)$ is a Gaussian distribution with zero-mean, $\pi_j$ is the mixture weight for the $j$'th mixture component, $\Sigma_j$ is the corresponding covariance matrix, $\mathbf{R}_i$ extracts the $i$'th patch of $\mathbf{s}$, and $\overline{\mathbf{R}_i\mathbf{s}}$ is the patch $\mathbf{R}_i\mathbf{s}$ with mean removed. We learn a 200 component GMM model with zero mean and full covariance matrices using a minibatch version of expectation maximization (EM),[58] the source code of which is publicly available.[59] As in Ref. 58, we iterate the EM update for 4000 times. At each iteration, we sample a $2 \times 10^5$ patches with a size of $8 \times 8$ from 167 training images. These images are from the RIT MCSL HDR Image Database[60] and the Funt et al. HDR dataset,[61] which have no overlap with the test images used in our experiments. We show in Fig. 5 the eigenvectors of six covariance matrices with the largest mixture weights from the learned GMM model.

$$M_3 = \begin{pmatrix} 0.15 & 0.56 & 0.00 & 0.00 & 0.22 & 0.07 & 0.00 & 0.00 & 0.00 & 0.00 & 0.00 & 0.00 & 0.00 & 0.00 & 0.00 & 0.00 \\ 0.00 & 0.00 & 0.00 & 0.00 & 0.00 & 0.00 & 0.49 & 0.32 & 0.00 & 0.00 & 0.14 & 0.05 & 0.00 & 0.00 & 0.00 & 0.00 \\ 0.00 & 0.00 & 0.00 & 0.00 & 0.15 & 0.00 & 0.00 & 0.00 & 0.74 & 0.00 & 0.00 & 0.00 & 0.11 & 0.00 & 0.00 & 0.00 \\ 0.00 & 0.00 & 0.00 & 0.00 & 0.00 & 0.00 & 0.00 & 0.00 & 0.00 & 0.00 & 0.00 & 0.00 & 0.00 & 0.50 & 0.50 & 0.00 \end{pmatrix}$$

**Fig. 4** An illustration of the coefficient matrix that maps a square layout into a Penrose one (adapted from Ref. 41).

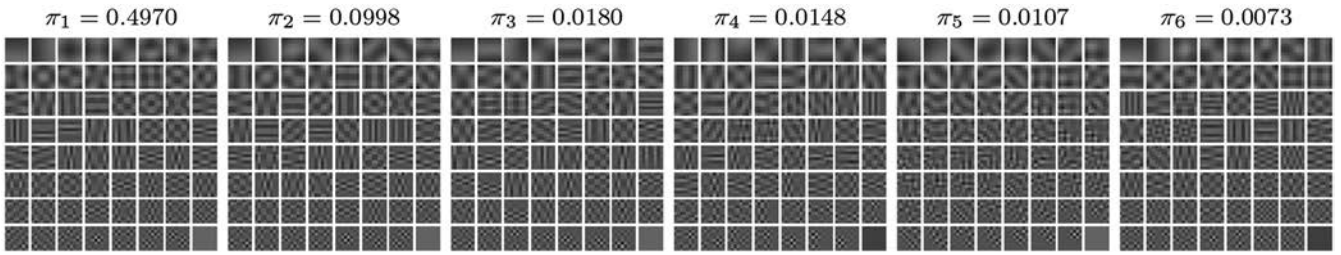


**Fig. 5** Eigenvectors of six covariance matrices with the largest mixture weights from the learned GMM model, sorted by eigenvalues from the largest to the smallest.

Since smooth regions occupy a very large proportion of an HDR image, especially those corresponding to the bright and the dark areas of the scene, we also include a non-negativity constraint for each pixel of $\mathbf{s}$. The non-negativity constraint has been shown very useful in regularizing the low frequencies.[62] So, our Penrose HDR model is finally formulated as

$$\min_{\mathbf{s}} \frac{\lambda}{2}\|\mathbf{U}(\mathbf{MTs}-\mathbf{p})\|_2^2 - \sum_i \log[\mathrm{GMM}(\mathbf{R}_i\mathbf{s})] \quad \text{s.t.}\mathbf{0} \le \mathbf{s} \le \mathbf{1}, \tag{7}$$

where $\lambda > 0$ is the parameter to balance the fidelity term and the regularization term, $\le$ stands for componentwise less than or equal to, $\mathbf{0}$ denotes the all-zero column vector, and $\mathbf{1}$ denotes the all-one column vector.

### 3.4 *Solving the Penrose High-Dynamic-Range Model*

The optimization problem [Eq. (7)] is nonconvex due to the use of the GMM prior. Following Ref. 42, we use the half-quadratic splitting scheme[63] to solve it. We first introduce an auxiliary variable $\mathbf{z}_i$ for each $\mathbf{R}_i\mathbf{s}$ and rewrite Eq. (7) as

$$\min_{\mathbf{s},\{\mathbf{z}_i\}} \frac{\lambda}{2}\|\mathbf{U}(\mathbf{MTs}-\mathbf{p})\|_2^2 + \frac{\beta}{2}\sum_i \|\mathbf{R}_i\mathbf{s}-\mathbf{z}_i\|_2^2 - \sum_i \log[\mathrm{GMM}(\mathbf{z}_i)], \text{s.t.}\mathbf{0} \le \mathbf{s} \le \mathbf{1}, \tag{8}$$

where $\beta$ is an increasing parameter to ensure that $\mathbf{R}_i\mathbf{s}$ gets closer to $\mathbf{z}_i$ along with the iterations.

Then by the half-quadratic splitting scheme, Eq. (8) can be solved via the following iterations:

$$\mathbf{s}^{l+1} = \operatorname*{argmin}_{\mathbf{0}\le\mathbf{s}\le\mathbf{1}} \frac{\lambda}{2}\|\mathbf{U}(\mathbf{MTs}-\mathbf{p})\|_2^2 + \frac{\beta^l}{2}\sum_i \|\mathbf{R}_i\mathbf{s}-\mathbf{z}_i^l\|_2^2, \tag{9}$$

$$\{\mathbf{z}_i^{l+1}\} = \operatorname*{argmin}_{\{\mathbf{z}_i\}} \frac{\beta^l}{2}\sum_i \|\mathbf{R}_i\mathbf{s}^{l+1}-\mathbf{z}_i\|_2^2 - \sum_i \log[\mathrm{GMM}(\mathbf{z}_i)], \tag{10}$$

$$\beta^{l+1} = \eta\beta^l. \tag{11}$$

We solve Eq. (9) as follows. Since Eq. (9) has box constraints, we use L-BFGS-B[64] to solve it (We download the C version of L-BFGS-B from Ref. 65). We only need to provide the objective function of Eq. (9) as well as its gradient w.r.t. $\mathbf{s}$. The calculation of this objective function is trivial and the gradient can be computed as

$$\lambda\mathbf{T}^T\mathbf{M}^T\mathbf{U}^T\mathbf{U}(\mathbf{MTs}-\mathbf{p}) + \beta^l\sum_i \mathbf{R}_i^T(\mathbf{R}_i\mathbf{s}-\mathbf{z}_i^l). \tag{12}$$

The only difference in applying our method with linear and nonlinear response functions is the computation of this gradient. We solve Eq. (10) as follows. Equation (10) does not have a closed-form solution. As suggested by Ref. 42, we use an approximate optimization to solve it. All the patches are independent of each other and hence can be processed in parallel. For each patch $\mathbf{R}_i\mathbf{s}^{l+1}$, we denote its mean pixel value as $v_i$ and the corresponding mean removed patch as $\overline{\mathbf{R}_i\mathbf{s}^{l+1}}$. We first calculate the assignment probability of $\overline{\mathbf{R}_i\mathbf{s}^{l+1}}$ to each of the $K$ mixture components. Then, we select the mixture component $k_{\max}$ with the largest assignment probability in the GMM model. We next perform Weiner filtering using only the $k_{\max}$'th component and then add the mean pixel value back

$$\mathbf{z}_i^{l+1} = (\Sigma_{k_{\max}} + \mathbf{I}/\beta^l)^{-1}(\Sigma_{k_{\max}}\overline{\mathbf{R}_i\mathbf{s}^{l+1}}) + v_i\mathbf{1},$$

where $\mathbf{I}$ is the identity matrix and $\Sigma_{k_{\max}}$ is the covariance matrix of the $k_{\max}$'th mixture component.

The update of $\beta$ in Eq. (11) is also very important. We set $\lambda = \tilde{\lambda}\times(8\times 8)/\tau$ to account for the varying $\mathbf{U} = \mathrm{diag}(\mathbf{u})$, where $8\times 8$ is the patch size, and $\tau$ is the ratio of nonzero elements in $\mathbf{u}$. In all our experiments, we set $\tilde{\lambda} = 2.5\times 10^3$, $\eta = 2$, and $\beta^0 = 100$ and iterate [Eqs. (9)–(11)] for 20 times.

Since the optimization problem [Eq. (8)] is nonconvex, a good initialization is important for achieving a good local minimum. We initialize the GMM-based model with the smoothness prior and non-negativity constraints

$$\mathbf{s}^0 = \operatorname*{argmin}_{\mathbf{s}} \frac{\mu}{2}\|\mathbf{U}(\mathbf{MTs}-\mathbf{p})\|_2^2 + \frac{1}{2}(\|\mathbf{G}_h\mathbf{s}\|_2^2 + \|\mathbf{G}_v\mathbf{s}\|_2^2) \quad \text{s.t.}\mathbf{0} \le \mathbf{s} \le \mathbf{1}, \tag{13}$$

where $\mathbf{G}_h$ and $\mathbf{G}_v$ are the convolution matrices corresponding to the partial derivative filters $\mathbf{g}_h = (-1,1)$ and $\mathbf{g}_v = (-1,1)^T$, respectively. We set $\mu = 2/\tau$ in all our experiments, where $\tau$ is the ratio of nonzero elements in $\mathbf{u}$ and $\mathbf{U} = \mathrm{diag}(\mathbf{u})$. We also use L-BFGS-B to solve Eq. (13). Then each auxiliary variable $\mathbf{z}_i$ in Eq. (9) is initialized as $\mathbf{z}_i^0 = \mathbf{R}_i\mathbf{s}^0$. A comparison of the GMM and the smoothness priors is shown in Fig. 6. We can see that the GMM prior can effectively remove sensor noise and well preserve the image sharpness.

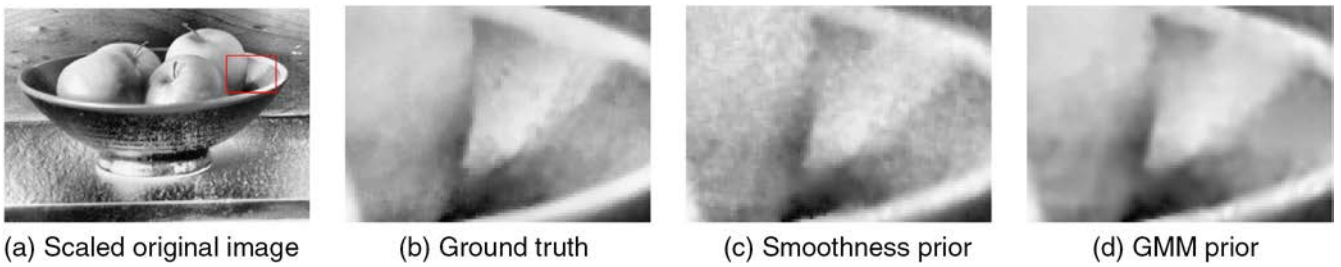


**Fig. 6** Comparison of the GMM and the smoothness priors. (a) The scaled original HDR image, in which the red rectangle indicates the selected patch to blow up, (b) the ground truth, and (c) and (d) the reconstructed HDR patches with the smoothness and the GMM priors, respectively.

We implement our reconstruction method in MATLAB®. With our unoptimized codes, the whole reconstruction method including the initialization process takes about 49 min to restore an image of size $1000 \times 1000$ pixels on a 4.00-GHz quad core machine.

## 4 Experiments

In this section, we test our irregular Penrose layout on synthetic images and compare it with a regular SVE array in the square layout. The regular SVE array is based on the Bayer CFA,[30] where three colors are replaced by three different sensitivities [see Fig. 1(b)]. So its sampling rate of the median sensitivity is twice as those of the low and high ones.

In addition, to understand the benefits of irregular pixel of the Penrose layout, we also include comparison with a random SVE array in square layout, which is based on the random CFA[27] [see Fig. 2(g)]. We choose it for comparison because it is random (and hence also aperiodic) and uniformly assigns three sensitivities. The only difference from the Penrose layout is that it uses square pixels.

We want to note that the reconstruction methods also highly affect the quality of HDR images. However, an extensive comparison of reconstruction methods is out of the scope of this work, so we use only the proposed method to compare all these SVE arrays.

### 4.1 *Experimental Settings*

#### 4.1.1 *Simulation of Penrose spatially varying exposures images*

Since the imaging sensor in the Penrose layout has not been manufactured, we need to simulate it. We first generate a Penrose layout that has the same resolution as the square layout, which has been detailed in Ref. 41. Then, we use the coloring algorithm proposed by Sibley and Wagon[66] to assign the three sensitivities. Our empirical tests show that this assignment of three sensitivities is approximately uniform. We simulate the Penrose SVE imaging as follows (Fig. 3). We first choose a gray-scale HDR image, which is also the ground truth, to simulate the scene [Fig. 3(a)]. Then, we expose the HDR image with three different exposures [Fig. 3(b)]. For each of the three differently exposed images, we obtain the corresponding subimage of the noiseless Penrose SVE image using Eq. (3) [Fig. 3(c)]. Following Ref. 33, we add the Poisson–Gaussian noise[54] at the ISO 800 setting to the noiseless Penrose SVE image to simulate the sensor noise. According to Eq. (2), the radiance values of the noisy image are converted into gray levels. We quantize the gray levels into 12 bits to finally obtain the Penrose SVE image. Then, we compute the corresponding proper exposure matrix $\mathbf{U}$ by Eq. (4). The simulation of SVE process for the square layout is exactly the same. The only difference is the layout mapping from Figs. 3(b) and 3(c). For square layout, the layout mapping is simply a subsampling process, i.e., drawing pixels from three differently exposed images as specified by the SVE array.

The noise model for each pixel of SVE images is[54]

$$y = x + e_p(x) + e_g,$$

where $y$ is the observed noisy pixel value in the SVE image, $x$ is the noiseless pixel value, $e_p(x)$ is the signal-dependent Poisson noise term, and $e_g$ is the signal-independent Gaussian noise term. The distributions of the two noise components are as follows:

$$x + e_p(x) \sim aP(x/a), e_g \sim N(0, b),$$

where $P$ and $N$ denote the Poisson and Gaussian distributions, respectively, and $a > 0$ and $b > 0$ are parameters. For pixel values between 0 and 1, $a = 0.0018679$ and $b = 3.3089 \times 10^{-5}$ correspond to the ISO 800 setting.[54]

Another important issue is the setting of three exposures as well as the reliable gray level range of the imaging sensor, i.e., $\{t_i\}_{i=1}^3$, $B_{\min}$, and $B_{\max}$ in Eq. (2). We determine these parameters based on a given ratio $\rho$ of the dark and bright areas in the scene, where the dark and bright ones have equal proportions. For an HDR image $\mathbf{s}$, which simulates the scene, we first sort all its $n$ radiance values in ascending order to have $\tilde{\mathbf{s}}$, where $\tilde{\mathbf{s}}(1) = I_{\min}$ and $\tilde{\mathbf{s}}(n) = I_{\max}$. Then, we set $B_{\min} = \tilde{\mathbf{s}}[\text{round}(n\rho/2)]$ and $B_{\max} = \tilde{\mathbf{s}}\{\text{round}[n(1-\rho/2)]\}$, where round $(\cdot)$ is the rounding operator. We next set the three exposures as follows:

$$\begin{cases} t_1 = B_{\max}/I_{\max}, \\ t_2 = 1, \\ t_3 = B_{\min}/I_{\min}, \end{cases} \tag{14}$$

where $t_1$ and $t_3$ exactly map $I_{\max}$ and $I_{\min}$ into the gray level range of the imaging sensor, respectively. This implies that the pixels of $\mathbf{s}$, whose values are less than or equal to $B_{\min}$, are regarded as the components of the dark scene areas, whereas the values of which are greater than or equal to $B_{\max}$ belong to the bright areas. As shown in Fig. 7, the larger $\rho$ is, the more pixels will be categorized into the dark and bright scene areas. It should be noted that we use $\rho$ to divide the scene into the dark, median, and bright areas. It is not the ratio of improperly exposed pixels indicated by $\mathbf{u}$ [see Eq. (4)].

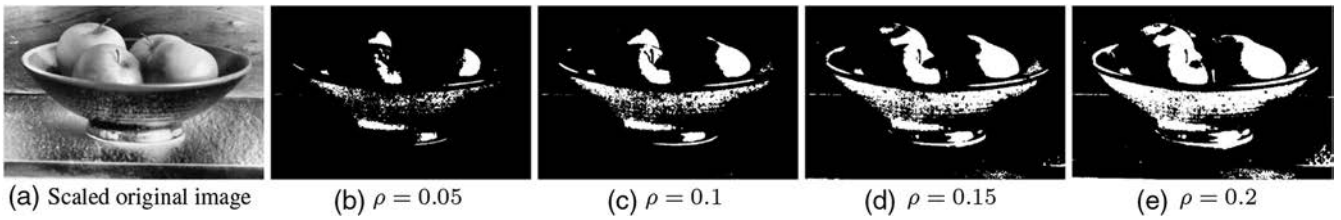


**Fig. 7** Correspondence between $\rho$ and the dark and bright areas in the scene (indicated by the white pixels).

#### 4.1.2 *Dataset and evaluation metrics*

We select nine HDR images from the RIT MCSL HDR Image Database[60] and the Funt et al. HDR Dataset[61] for the test, and the remaining 167 images of the two datasets for training. (Note that the Funt et al. HDR dataset consists of paired images. One has a Colorchecker in it and the other does not. We use only the images without Colorcheckers in them.). We first crop a region with a large dynamic range from each of the nine images, the sizes of which vary among $1000 \times 1000$, $512 \times 768$, and $391 \times 587$. Then, we transform the cropped images from the RGB to the YIQ color spaces using MATLAB®'s default `rgb2ntsc` function. We use only the luminance channel of each YIQ image as the HDR image, which is also the ground truth. Figure 8 shows all nine images used in our test.

There are some subjective and objective image quality measures that have been proposed.[67,68] Following most of the existing literature in SVE imaging,[24,25,31–33] we use PSNR to measure the performance: $\mathrm{PSNR}(\hat{\mathbf{x}}, \mathbf{x}) = 10\log_{10}(n/\|\hat{\mathbf{x}} - \mathbf{x}\|_2^2)$, where $\mathbf{x}$ is the ground truth and its radiance values are between 0 and 1, $\hat{\mathbf{x}}$ is its reconstruction, and $n$ is the number of elements in $\mathbf{x}$. Note that $\mathbf{x}$ can be formed by either all the radiance values or the selected ones of an HDR image. We also compare the HDR results by visual evaluation.

### 4.2 *Comparison with Regular Spatially Varying Exposures Array*

We first compare Penrose SVE array with the regular one in the square layout under four different settings of $\rho$. Table 1 shows the individual and average PSNR values of regular and Penrose SVE arrays on all test images. The corresponding percentage of unknown pixels [improperly exposed pixels indicated by $\mathbf{u}$ Eq. (4)] for each scenario is shown in Fig. 9.

**Fig. 8** The test HDR images used in our experiments. These images are numbered from 1 to 9 in the order of left to right and top to bottom.

Since the regular SVE array has twice the median exposures as the low and high ones [see Fig. 1(b)], we can see that it always results in fewer unknown pixels. Nonetheless, in terms of PSNR, we can see that Penrose SVE array outperforms the regular one for every $\rho$ on both individual image and the whole test images, being only slightly inferior on the #9 image under $\rho = 0.05$ (indicated by italics in Table 1).

We present part of the visual comparison in Figs. 10–13. We can see that the visual quality of Penrose HDR images is better than that of the regular ones, especially in reconstructing highly contrasted edges (read the captions for the descriptions on visual difference).

### 4.3 *Effectiveness of Irregular Pixels*

We have shown that the Penrose layout can produce high-quality HDR images. We are also interested in investigating whether this benefits from the irregularity of the Penrose layout. In this section, we further compare Penrose SVE array with a random one in the square layout. As mentioned earlier, it is based on the random CFA[27] [see Fig. 2(g)] and uniformly randomly assigns the three sensitivities. The only difference from the Penrose SVE array is that it uses square pixels. Accordingly, we can see from Fig. 9 that the random SVE array always results in identical percentages of unknown pixels as the Penrose one does.

From Table 1, we can see that the Penrose SVE array is slightly inferior to the random one when $\rho = 0.05$. However, the Penrose SVE array significantly outperforms the random one under the other three settings of $\rho$ and the superiority increases with the value of $\rho$. One possible reason is that the random SVE array has inherent advantage in PSNR, particularly when the percentage of unknown pixels is small. This is because we use an HDR image in a square layout to simulate the scene and PSNR is based on computing the pixel-wise difference between the reconstructed image and the ground truth. For the ideal imaging case, there is no noise and every pixel in the SVE image is properly exposed. Then, for the square layout, the normalized SVE image by respective exposures of all pixels is identical to the ground truth, i.e., the SVE imaging is invertible. For the Penrose layout, however, the invertibility is true only in theory. The simulation error of layout mapping always exists in real computation. Nonetheless, when we compare the visual quality in Figs. 10–13, the Penrose SVE array is better at reconstructing fine details than the random one is.

To further test the performance of the Penrose layout, we also compute PSNR values only on the dark and bright scene

**Table 1** PSNR values on the whole images. The individual and average PSNR values are reported. For each $\rho$, the best values are in boldface.

| | $\rho = 0.05$ | | | $\rho = 0.1$ | | | $\rho = 0.15$ | | | $\rho = 0.2$ | | |
|---|---|---|---|---|---|---|---|---|---|---|---|---|
| Image ID | Regular | Random | Penrose | Regular | Random | Penrose | Regular | Random | Penrose | Regular | Random | Penrose |
| 1 | 37.79 | 38.23 | **38.37** | 36.81 | 37.57 | **37.98** | 35.45 | 35.86 | **36.67** | 33.43 | 33.60 | **34.63** |
| 2 | 39.06 | 39.07 | **39.20** | 38.62 | 38.71 | **38.89** | 37.86 | 37.77 | **38.24** | 35.89 | 35.58 | **36.29** |
| 3 | 37.71 | **38.27** | 38.15 | 36.93 | **37.68** | 37.67 | 36.01 | 36.42 | **36.79** | 33.81 | 33.82 | **34.75** |
| 4 | 35.82 | 35.96 | **36.03** | 34.69 | 35.34 | **35.71** | 34.00 | 34.97 | **35.47** | 33.06 | 33.87 | **34.74** |
| 5 | 38.62 | **39.02** | 38.80 | 37.59 | **38.49** | 38.29 | 36.82 | **37.70** | 37.64 | 35.79 | 36.35 | **36.72** |
| 6 | 36.71 | **36.81** | 36.79 | 36.45 | 36.54 | **36.61** | 35.92 | 36.03 | **36.18** | 34.65 | 34.75 | **35.05** |
| 7 | 35.42 | 35.25 | **35.65** | 31.94 | 31.57 | **32.50** | 29.62 | 29.25 | **30.11** | 27.87 | 27.39 | **28.27** |
| 8 | 38.08 | **38.35** | 38.27 | 37.56 | 37.90 | **37.94** | 37.19 | 37.67 | **37.73** | 36.93 | 37.44 | **37.63** |
| 9 | 37.75 | **38.13** | *37.72* | 33.69 | 33.61 | **34.71** | 29.34 | 29.29 | **30.44** | 25.96 | 26.07 | **26.68** |
| Average | 37.77 | **38.18** | 38.05 | 35.25 | 35.59 | **36.35** | 32.39 | 32.57 | **33.55** | 29.69 | 29.83 | **30.66** |

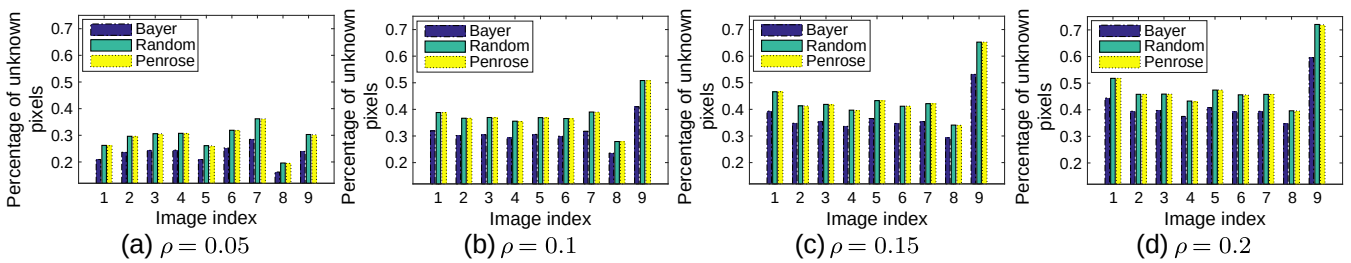


**Fig. 9** The percentage of unknown pixels of each compared SVE array with varying $\rho$.

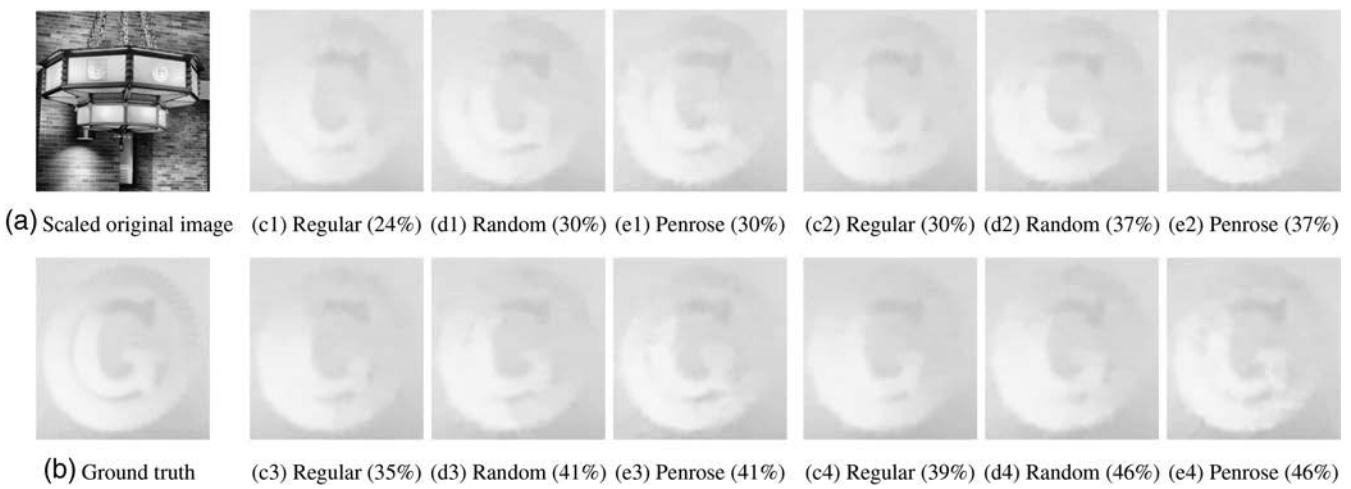


**Fig. 10** One blowup of the reconstructed #2 image with varying $\rho$. (a)The scaled original image, in which the red rectangle indicates the selected patch to blow up, (b) the ground truth. From groups 1 to 4, the $\rho$ are 0.05, 0.1, 0.15, and 0.2, respectively. In each group, (c)–(e) are the HDR images reconstructed from regular, random, and Penrose SVE images, respectively, where the percentages are the unknown pixel ratios of these SVE images. Note the space between the circle and the large character "G."

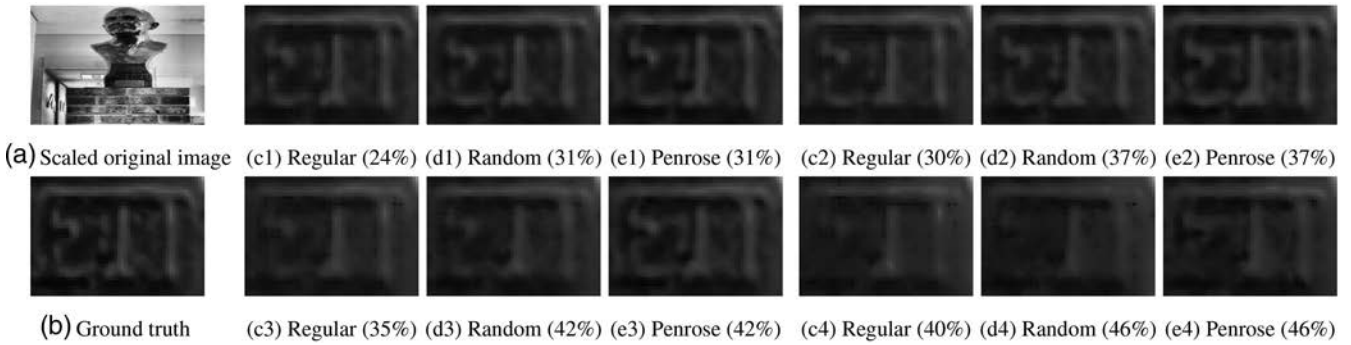


**Fig. 11** One blowup of the reconstructed #3 image with varying $\rho$. The notations are the same as those in Fig. 10. The characters are "ETT." Note the character "E."

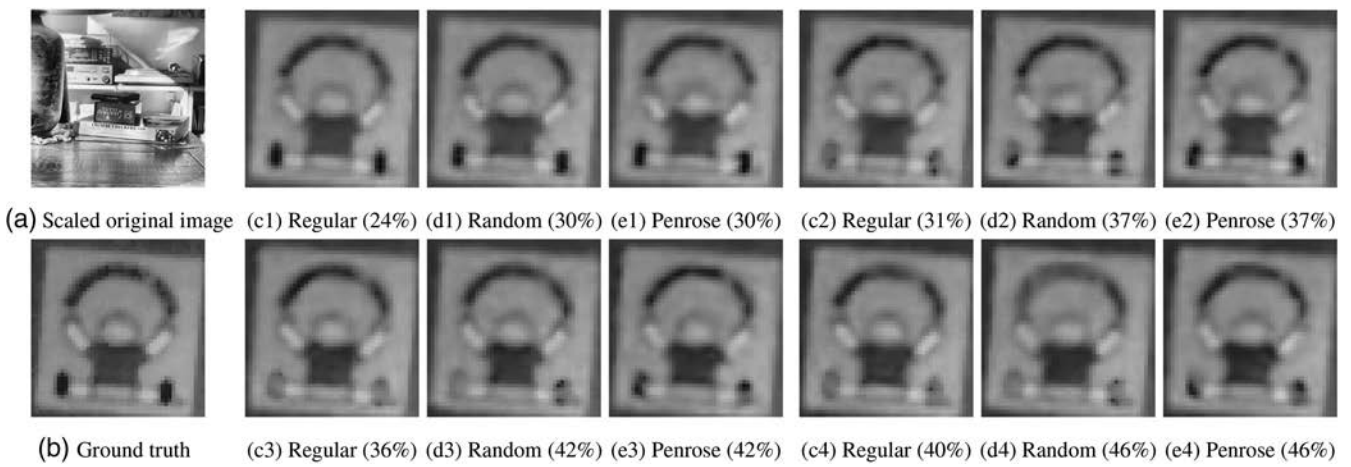


**Fig. 12** One blowup of the reconstructed #7 image with varying $\rho$. The notations are the same as those in Fig. 10. Note the feet of the cartoon character.

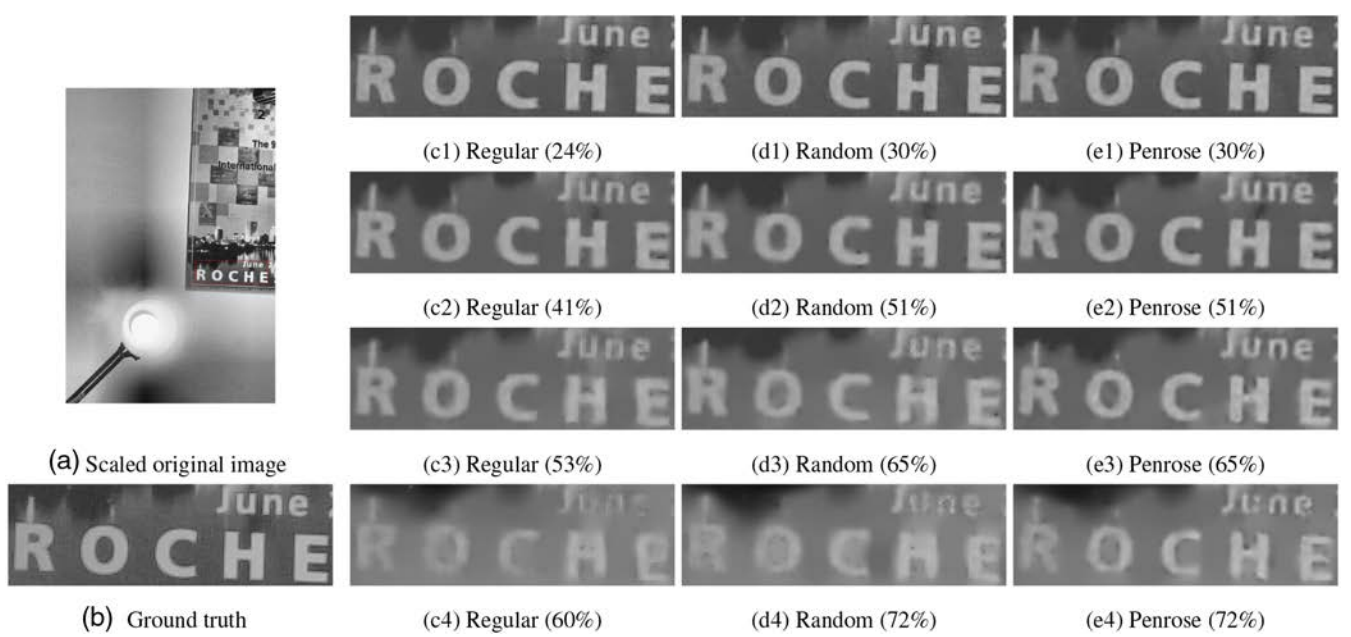


**Fig. 13** One blowup of the reconstructed #9 image with varying $\rho$. The notations are the same as those in Fig. 10. Note the characters.

**Table 2** PSNR values on the bright and dark regions of the images. The individual and average PSNR values are reported. For each $\rho$, the best values are in boldface.

| | $\rho = 0.05$ | | | $\rho = 0.1$ | | | $\rho = 0.15$ | | | $\rho = 0.2$ | | |
|---|---|---|---|---|---|---|---|---|---|---|---|---|
| Image ID | Regular | Random | Penrose | Regular | Random | Penrose | Regular | Random | Penrose | Regular | Random | Penrose |
| 1 | 42.29 | 43.97 | **45.76** | 40.07 | 42.20 | **43.95** | 38.17 | 39.76 | **41.23** | 35.01 | 35.64 | **36.97** |
| 2 | 47.23 | 49.24 | **50.67** | 45.46 | 47.66 | **48.75** | 43.44 | 45.17 | **46.56** | 38.84 | 39.13 | **40.04** |
| 3 | 43.08 | 46.22 | **47.76** | 41.22 | 44.26 | **45.74** | 39.81 | 42.09 | **43.18** | 35.74 | 36.31 | **37.67** |
| 4 | 41.48 | 42.99 | **45.38** | 38.20 | 40.45 | **42.99** | 36.77 | 39.41 | **41.77** | 35.16 | 37.02 | **39.28** |
| 5 | 44.72 | 47.31 | **48.46** | 41.82 | 44.94 | **45.74** | 40.37 | 43.54 | **43.80** | 38.48 | 40.41 | **41.16** |
| 6 | 43.80 | 45.95 | **47.69** | 42.46 | 44.43 | **45.79** | 40.74 | 42.62 | **43.46** | 37.58 | 38.56 | **39.02** |
| 7 | 39.06 | 39.12 | **40.31** | 33.23 | 32.88 | **34.17** | 30.33 | 29.99 | **30.98** | 28.33 | 27.88 | **28.81** |
| 8 | 45.05 | 46.79 | **47.92** | 43.19 | 45.06 | **46.38** | 42.04 | 44.26 | **45.31** | 41.30 | 43.56 | **44.63** |
| 9 | 42.50 | 44.46 | **45.02** | 35.65 | 36.49 | **38.01** | 29.94 | 30.05 | **31.34** | 26.23 | 26.38 | **27.03** |
| Average | 42.40 | 44.21 | **45.39** | 37.86 | 39.34 | **40.98** | 34.06 | 34.91 | **36.28** | 30.62 | 31.01 | **32.00** |

areas (indicated by the white pixels in Fig. 7), where the spatial resolutions are highly reduced. The individual and average PSNR values are shown in Table 2. We can see that the Penrose SVE array significantly outperforms the other ones on both individual image and the whole test images.

These experiments testify that the irregularity of Penrose SVE array is important for preventing the loss of resolution in the reconstructed HDR images, especially those image regions that correspond to the dark and bright scene areas.

The effectiveness of irregular pixels can be explained as follows. For the square layout, every to-be-reconstructed square pixel is either completely covered by a known square SVE pixel or not covered by any known square SVE pixel. For the Penrose layout, almost every to-be-reconstructed square pixel is partly covered by a known irregular SVE pixel [see Fig. 3(c)]. Accordingly, for the square layout, the unknown pixel completely loses its information. In contrast, irregular SVE array results in less information loss as the captured value of every Penrose pixel is always a mixture of those of nearby square pixels [see Fig. 3(c)]. It can also be understood as that every square pixel is contributed by multiple Penrose pixels that jointly cover it, which often contain at least one known Penrose pixel value. That is why the Penrose layout can better capture the dark and bright areas of the scene.

## 5 Conclusions

In this paper, we present the Penrose layout for HDR imaging using the SVE technology, making it aperiodic in both exposure and pixel arrangements. Since the Penrose layout is irregular and aperiodic, the existing HDR reconstruction methods are not applicable to it. We develop an HDR reconstruction method with a GMM model for regularization. Extensive experiments show that the Penrose layout is advantageous in alleviating the reduction in spatial resolution of the reconstructed HDR images.


### Acknowledgments

The work of Chenyan Bai was partially supported by the Fundamental Research Funds for the Central Universities under Grant No. K16JB00080. The work of Zhouchen Lin was partially supported by the 973 Program of China under Grant No. 2015CB352502, partially by the National Natural Science Foundation of China (NSFC) under Grant Nos. 61272341 and 61231002, and partially by the Microsoft Research Asia Collaborative Research Program. The work of Jian Yu was partially supported by the NSFC under Grant No. 61370129 and the PhD Programs Foundation of Ministry of Education of China under Grant No. 20120009110006.


### References


1. E. Reinhard et al., *High Dynamic Range Imaging: Acquisition, Display, and Image-Based Lighting*, Morgan Kaufmann, Burlington, Massachusetts (2010).
2. S. Mann and R. W. Picard, "On being 'undigital' with digital cameras: extending dynamic range by combining differently exposed pictures," in *Proc. of IS&T's 48th Annual Conf.*, pp. 442–448 (1995).
3. P. E. Debevec and J. Malik, "Recovering high dynamic range radiance maps from photographs," in *Proc. SIGGRAPH* (1997).
4. T. Mitsunaga and S. K. Nayar, "Radiometric self calibration," in *Proc. of IEEE Computer Society Conf. on Computer Vision and Pattern Recognition*, Vol. 1, IEEE (1999).
5. G. Ward, "Fast, robust image registration for compositing high dynamic range photographs from hand-held exposures," *J. Graphics Tools* **8**(2), 17–30 (2003).
6. A. Tomaszewska and R. Mantiuk, "Image registration for multi-exposure high dynamic range image acquisition," in *Proc. of Int. Conf. in Central Europe on Computer Graphics and Visualization* (2007).
7. J. Hu et al., "HDR deghosting: how to deal with saturation?" in *Proc. of IEEE Conf. on Computer Vision and Pattern Recognition*, pp. 1163–1170, IEEE (2013).

8. S. W. Hasinoff, F. Durand, and W. T. Freeman, "Noise-optimal capture for high dynamic range photography," in *Proc. of IEEE Conf. on Computer Vision and Pattern Recognition*, pp. 553–560, IEEE (2010).
9. M. Granados et al., "Optimal HDR reconstruction with linear digital cameras," in *Proc. of IEEE Conf. on Computer Vision and Pattern Recognition*, pp. 215–222, IEEE (2010).
10. K. Hirakawa and P. J. Wolfe, "Optimal exposure control for high dynamic range imaging," in *Proc. of IEEE Int. Conf. on Image Processing*, pp. 3137–3140, IEEE (2010).
11. M. Gupta, D. Iso, and S. K. Nayar, "Fibonacci exposure bracketing for high dynamic range imaging," in *Proc. of IEEE Int. Conf. on Computer Vision*, pp. 1473–1480, IEEE (2013).
12. R. Pourreza-Shahri and N. Kehtarnavaz, "Exposure bracketing via automatic exposure selection," in *Proc. of IEEE Int. Conf. on Image Processing*, pp. 320–323, IEEE (2015).
13. A. Agarwala et al., "Interactive digital photomontage," *ACM Trans. Graphics* **23**(3), 294–302 (2004).
14. E. A. Khan, A. Akyiiz, and E. Reinhard, "Ghost removal in high dynamic range images," in *Proc. of IEEE Int. Conf. on Image Processing*, pp. 2005–2008, IEEE (2006).
15. P. Sen et al., "Robust patch-based HDR reconstruction of dynamic scenes," *ACM Trans. Graphics* **31**(6), 203 (2012).
16. C. Lee, Y. Li, and V. Monga, "Ghost-free high dynamic range imaging via rank minimization," *IEEE Signal Process. Lett.* **21**(9), 1045–1049 (2014).
17. O. T. Tursun et al., "The state of the art in HDR deghosting: a survey and evaluation," *Proc. Comput. Graphics Forum* **34**, 683–707 (2015).
18. K. Jacobs, C. Loscos, and G. Ward, "Automatic high-dynamic range image generation for dynamic scenes," *IEEE Comput. Graphics Appl.* **28**(2), 84–93 (2008).
19. T.-H. Oh et al., "Robust high dynamic range imaging by rank minimization," *IEEE Trans. Pattern Anal. Mach. Intell.* **37**(6), 1219–1232 (2015).
20. N. K. Kalantari et al., "Patch-based high dynamic range video," *ACM Trans. Graphics* **32**(6), 202 (2013).
21. S. K. Nayar and T. Mitsunaga, "High dynamic range imaging: spatially varying pixel exposures," in *Proc. of IEEE Conf. on Computer Vision and Pattern Recognition*, Vol. 1, pp. 472–479, IEEE (2000).
22. Fujifilm Corporation, "The 4th-generation super CCD," 21 January 2003, https://www.fujifilmusa.com/shared/bin/4thGenSUPERCCDBrochure.pdf (10 January 2015).
23. Sony Corporation, "Image processing apparatus, image processing method, and program," 30 October 2014, http://www.freepatentsonline.com/20140321766.pdf (10 January 2015).
24. M. Schöberl et al., "High dynamic range video by spatially non-regular optical filtering," in *Proc. of IEEE Int. Conf. on Image Processing*, (2012).
25. C. Aguerrebere et al., "Single shot high dynamic range imaging using piecewise linear estimators," in *Proc. of IEEE Int. Conf. on Computational Photography*, pp. 1–10, IEEE (2014).
26. H. Cho, S. J. Kim, and S. Lee, "Single-shot high dynamic range imaging using coded electronic shutter," *Comput. Graphics Forum* **33**(7), 329–338 (2014).
27. L. Condat, "Color filter array design using random patterns with blue noise chromatic spectra," *Image Vision Comput.* **28**(8), 1196–1202 (2010).
28. M. Mase et al., "A wide dynamic range CMOS image sensor with multiple exposure-time signal outputs and 12-bit column-parallel cyclic A/D converters," *IEEE J. Solid-State Circuits* **40**(12), 2787–2795 (2005).
29. J. Gu et al., "Coded rolling shutter photography: flexible space-time sampling," in *Proc. of IEEE Int. Conf. on Computational Photography*, pp. 1–8 (2010).
30. B. E. Bayer, "Color imaging array," U.S. Patent No. 3,971,065 (1976).
31. S. G. Narasimhan and S. K. Nayar, "Enhancing resolution along multiple imaging dimensions using assorted pixels," *IEEE Trans. Pattern Anal. Mach. Intell.* **27**(4), 518–530 (2005).
32. M. V. Konnik, E. A. Manykin, and S. N. Starikov, "Optical-digital correlator with increased dynamic range using spatially varying pixels exposure technique," *Opt. Mem. Neural Networks* **18**(2), 61–71 (2009).
33. K. Hirakawa and P. M. Simon, "Single-shot high dynamic range imaging with conventional camera hardware," in *Proc. of IEEE Int. Conf. on Computer Vision*, pp. 1339–1346, IEEE (2011).
34. D. Alleysson, S. Susstrunk, and J. Hérault, "Linear demosaicing inspired by the human visual system," *IEEE Trans. Image Process.* **14**(4), 439–449 (2005).
35. T. Mitsa and K. J. Parker, "Digital halftoning technique using a blue-noise mask," *J. Opt. Soc. Am. A* **9**(11), 1920–1929 (1992).
36. J. I. Yellott, "Spectral analysis of spatial sampling by photoreceptors: topological disorder prevents aliasing," *Vision Res.* **22**(9), 1205–1210 (1982).
37. R. H. Kröger, "Anti-aliasing in image recording and display hardware: lessons from nature," *J. Opt. A Pure Appl. Opt.* **6**(8), 743–748 (2004).
38. B. Grfinbaum and G. Shephard, *Tilings and Patterns*, Freeman, New York, New York (1987).
39. F. Aurenhammer, "Voronoi diagrams: a survey of a fundamental geometric data structure," *ACM Comput. Surv.* **23**(3), 345–405 (1991).
40. M. Ben-Ezra et al., "Penrose pixels for super-resolution," *IEEE Trans. Pattern Anal. Mach. Intell.* **33**(7), 1370–1383 (2011).
41. C. Bai et al., "Penrose demosaicking," *IEEE Trans. Image Process.* **24**(5), 1672–1684 (2015).
42. D. Zoran and Y. Weiss, "From learning models of natural image patches to whole image restoration," in *Proc. of IEEE Int. Conf. on Computer Vision*, pp. 479–486, IEEE (2011).
43. J. Tumblin, A. Agrawal, and R. Raskar, "Why I want a gradient camera," in *Proc. of IEEE Computer Society Conf. on Computer Vision and Pattern Recognition*, Vol. 1, pp. 103–110, IEEE (2005).
44. H. Zhao et al., "Unbounded high dynamic range photography using a modulo camera," in *Proc. of IEEE Int. Conf. on Computational Photography*, pp. 1–10, IEEE (2015).
45. B. Zitova and J. Flusser, "Image registration methods: a survey," *Image Vision Comput.* **21**(11), 977–1000 (2003).
46. S. B. Kang et al., "High dynamic range video," *ACM Trans. Graphics* **22**(3), 319–325 (2003).
47. H. Zimmer, A. Bruhn, and J. Weickert, "Freehand HDR imaging of moving scenes with simultaneous resolution enhancement," *Comput. Graphics Forum* **30**(2), 405–414 (2011).
48. M. D. Grossberg and S. K. Nayar, "Determining the camera response from images: what is knowable?" *IEEE Trans. Pattern Anal. Mach. Intell.* **25**(11), 1455–1467 (2003).
49. Y. S. Heo et al., "Ghost-free high dynamic range imaging," in *Proc. of Asian Conf. on Computer Vision*, pp. 486–500, Springer (2011).
50. O. Gallo et al., "Artifact-free high dynamic range imaging," in *Proc. of IEEE Int. Conf. on Computational Photography*, pp. 1–7, IEEE (2009).
51. S. Raman and S. Chaudhuri, "Reconstruction of high contrast images for dynamic scenes," *Visual Comput.* **27**(12), 1099–1114 (2011).
52. W. Zhang and W.-K. Cham, "Gradient-directed multiexposure composition," *IEEE Trans. Image Process.* **21**(4), 2318–2323 (2012).
53. M. Granados et al., "Automatic noise modeling for ghost-free HDR reconstruction," *ACM Trans. Graphics* **32**(6), 201 (2013).
54. A. Foi et al., "Practical Poissonian–Gaussian noise modeling and fitting for single-image raw-data," *IEEE Trans. Image Process.* **17**(10), 1737–1754 (2008).
55. J. Seiler and A. Kaup, "Complex-valued frequency selective extrapolation for fast image and video signal extrapolation," *IEEE Signal Process. Lett.* **17**(11), 949–952 (2010).
56. G. Yu, G. Sapiro, and S. Mallat, "Solving inverse problems with piecewise linear estimators: from Gaussian mixture models to structured sparsity," *IEEE Trans. Image Process.* **21**(5), 2481–2499 (2012).
57. Z. Lin and H.-Y. Shum, "Fundamental limits of reconstruction-based superresolution algorithms under local translation," *IEEE Trans. Pattern Anal. Mach. Intell.* **26**(1), 83–97 (2004).
58. D. Zoran and Y. Weiss, "Natural images, Gaussian mixtures and dead leaves," in *Proc. of Advances in Neural Information Processing Systems*, pp. 1736–1744 (2012).
59. D. Zoran and Y. Weiss, "Mini-batch version of GMM,"08 December 2012, http://people.csail.mit.edu/danielzoran/ (15 January 2015).
60. Munsell Color Science Laboratory, "RIT MCSL high dynamic range image database," 23 March 2004, http://www.cis.rit.edu/research/mcsl2/icam/hdr/rit_hdr/ (10 January 2015).
61. B. Funt and L. Shi, "Funt et al. HDR Dataset," 16 November 2010, http://www.cs.sfu.ca/~colour/data/funt_hdr/ (10 January 2015).
62. Y. Shih et al., "Reflection removal using ghosting cues," in *Proc. of the IEEE Conf. on Computer Vision and Pattern Recognition*, pp. 3193–3201 (2015).
63. D. Geman and C. Yang, "Nonlinear image recovery with half-quadratic regularization," *IEEE Trans. Image Process.* **4**(7), 932–946 (1995).
64. C. Zhu et al., "Algorithm 778: L-BFGS-B: Fortran subroutines for large-scale bound-constrained optimization," *ACM Trans. Math. Softw.* **23**(4), 550–560 (1997).
65. S. Becker, "L-BFGS-B-C," 23 April 2015, https://github.com/stephenbeckr/L-BFGS-B-C (23 June 2015).
66. T. Sibley and S. Wagon, "Rhombic Penrose tilings can be 3-colored," *Am. Math. Mon.* **107**(3), 251–253 (2000).
67. Z. Wang and A. C. Bovik, "Mean squared error: love it or leave it? A new look at signal fidelity measures," *IEEE Signal Process. Mag.* **26**(1), 98–117 (2009).
68. R. Mantiuk et al., "HDR-VDP-2: a calibrated visual metric for visibility and quality predictions in all luminance conditions," *ACM Trans. Graphics* **30**(4), 40 (2011).


**Jia Li** received his bachelor's degree in mathematics and his master's degree in computer science from Zhengzhou University, Zhengzhou, China, in 2007 and 2012, respectively. He is currently pursuing his PhD at Beijing Key Laboratory of Traffic Data Analysis and Mining, School of Computer and Information Technology, Beijing Jiaotong University. His research interest is image processing.

**Chenyan Bai** received her bachelor's and master's degrees of engineering in computer science from the School of Mathematics and Computer Science, Hebei University, China, in 2008 and 2011,

respectively. She is currently pursuing her PhD at Beijing Key Laboratory of Traffic Data Analysis and Mining, School of Computer and Information Technology, Beijing Jiaotong University. Her research interest is image processing.

**Zhouchen Lin** received his PhD in applied mathematics from the Peking University in 2000. Currently, he is a professor at the Key Laboratory of Machine Perception (Ministry of Education), School of Electronic Engineering and Computer Science, Peking University. His research interests include computer vision, image processing, machine learning, pattern recognition, and numerical optimization. He is an associate editor of the *IEEE Transactions on Pattern Analysis and Machine Intelligence* and the *International Journal of Computer Vision*.

**Jian Yu** received his BS and MS degrees in mathematics and his PhD in applied mathematics from the Peking University, Beijing, China, in 1991, 1994, and 2000, respectively. He is currently a professor at Beijing Jiaotong University and the director of the Beijing Key Laboratory of Traffic Data Analysis and Mining. His research interests include machine learning, image processing, and pattern recognition.